Supplementary Materials for

Cutting muscle for bone regeneration

Xiaoyang Liu [1], Zhengke Wang [1*]

[1]MOE Key Laboratory of Macromolecular Synthesis and Functionalization

Department of Polymer Science and Engineering

Zhejiang University; Hangzhou, Zhejiang Province, 310058, China

E-mail: wangzk@zju.edu.cn

The PDF file includes:

Materials and Methods
Figs. S1 to S19
Tables S1
References

Other Supplementary Materials for this manuscript include the following:

Movies S1 to S8

Materials and Methods

Materials

Fresh pork tenderloin (purchased from Yijiahui supermarket) was chosen as a source of muscle fiber. NaCl, NaOH, acetone (≥99.5%), $CaCl_2$, were purchased from Sinopharm Chemical Reagent Co., Ltd. Guanidine hydrochloride, Sulfo-CY-5.5 NHS ester, and glutaraldehyde (50%, v/v) were supplied by Aladdin. NaH_2PO_4, alendronate monosodium trihydrate, rhodamine B were purchased from Macklin. Phosphate buffer saline (PBS) was provided by Biosharp, and the deionized water was supplied by Zhejiang University. All reagents were used as received without purification.

Pretreatment of muscle

The fresh pork tenderloin was cut into 20mm* 10mm* 2 mm slices, and placed in saline to remove residual blood. All muscle pieces were soaked in acetone overnight to remove lipids. After degreasing, the acetone in muscle was exchanged by deionized water. Then, muscle pieces were randomly divided into three groups, and treated with deionized water (DI), guanidine hydrochloride solution (GH, 2M) and NaOH solution (5wt%) for 3h, respectively, and named DI group, NaOH group, and GH group.

Mineralization of muscle

Prior to mineralization, all muscles were thoroughly washed to remove possible residual reagents. Muscles were immersed in $CaCl_2$ (0.2M), NaH_2PO_4 (0.12M), and alkaline water (pH~11) in sequence per 1h. Before soaked into alkaline water, muscles need to be immersed in NaOH solution (1wt%) for 5min. The cyclic mineralization terminated when the mineral content reached around 20wt% (NaOH group: 20.41%; GH group: 22.68%; DI group: 25.46%). The DI group and the GH group need cyclic mineralization for 7 times, while the NaOH group only needs 5 times. Mineralized muscles were frozen at -20 ℃ and lyophilized at -50 ℃ for 24h to obtain scaffolds.

Observation of mineralization process

After degreasing, muscle fiber was extracted, and laid flat on a slide. The variations of muscle fibers during mineralization process were observed by microscope. When replacing the mineralization liquid, filter paper was used to blot the last residual mineralization liquid, and then the new mineralization liquid was added.

Characterization of mineralized muscle

Fourier transform infrared spectroscopy (FTIR): The mineralized muscles are ground into powder after drying at 60 ℃. The FTIR spectra were measured on an attenuated total reflection-FTIR spectroscope (Nicolet 6700, Thermo, American), and the scanned wavenumber ranged from 4000 to 500 cm^{-1}.

Raman spectrum: Similar to observing the muscle fiber mineralization process, the muscle fiber was isolated from the mineralized muscle. The mineralization location was observed by linear scanning in aqueous environment. The Raman signal was collected by multichannel Raman spectrometer (Renishaw plc, inVia Reflex, 532 nm excitation).

Confocal laser scanning microscope (CLSM): To better visualize the distribution of hydroxyapatite in muscle, we labeled hydroxyapatite with Rhodamine B which modified by sodium alendronate, and labeled protein with Cy5.5 respectively. The mineralized muscle fibers after staining were observed by CLSM (LSM900, ZEISS, Germany).

Thermogravimetric analysis (TGA): The thermogravimetric curves were obtained through a thermogravimetric analyzer (TA-Q500, TA Instruments, American) from 25 ℃ to 850 ℃, using a heating rate of 10 ℃/min and air atmosphere.

X-ray diffraction (XRD): Similar to the pretreatment process in infrared spectroscopy testing, the mineralized muscle was ground into a powder after drying. The XRD patterns were acquired with X-ray diffractometer (Ultima IV, Rigaku Corporation, Japan) operated at 40 kV, 30 mA, and 25 °C (step size: 0.02).

Small angle X-ray scattering (SAXS): The mineralized muscle pieces were fixed on the sample holder of SAXS (Xeuss SAXs/WAXs System, Xenocs SA, France). The excillum METALJET liquid target was selected as the light source, and test power was 70 KV, 3.5 mA, 250 W.

X-ray photoelectron spectroscopy (XPS): The XPS spectra were scanned by x-ray photoelectron spectrometer (Thermo Scientific ESCALAB 250Xi, optical source: Al Ka 1486.6 eV). Full spectrum condition: pass energy: 100 eV, energy step size: 1 eV; Spectral scanning condition: pass energy: 20 eV, energy step size: 0.05 eV.

Scanning electron microscope (SEM): We used conductive glue to fix the mineralized muscle on the sample table, and exposed the fiber bundle cross section to the electron beam. The samples were sprayed with platinum, and observed using a scanning electron microscope (SU-3500, Hitachi, Japan). The distribution of C, N, Ca, and P was obtained by energy spectrometer (EDS, X-MAX 20, Oxford, England).

Transmission electron microscope (TEM): The mineralized muscles were cut into small pieces, and fixed with glutaraldehyde (2.5%, v/v). After gradient dehydration with ethanol, the samples were treated with acetone again. Next, the mineralized sample was embedded with resin (Spurr low viscosity embedding kit), and cured overnight at 70 ℃. The samples were sliced parallel and perpendicular to the muscle fibers, respectively, and the mineral distribution in the muscle was observed under TEM (HT7800, Hitachi, Japan).

Atomic force microscope (AFM): Considering the high requirement of the sample flatness of AFM (Cypher ES, Oxford, England), we directly selected the sample on TEM copper grids for testing. The surface morphology of the slice was obtained by AFM tapping mode, and the mechanical properties of the samples were deduced according to the adhesion force.

Microcomputed tomography (micro-CT): To image the mineralized muscle in three dimensions, the samples were scanned with an X-ray microcomputed tomography apparatus (U-CT-XUHR, Milabs, Netherlands).

Bone regeneration *in vivo*

All procedures related to animal feeding and surgery were conformed with the relevant laws, and authorized by the Institutional Animal Care and Use Committee (ZJCLA-IACUC-20020216). Considering the anisotropy of bone and muscle, we built a rabbit femur defect model to evaluate the effect of different mineralization pretreatments of muscle fibers on bone repair performance. This study was divided into 5 groups (blank control group, pure muscle group, DI group, GH group, and NaOH group), and a total of 62 healthy male rabbits (weighing 2.5 kilograms) were used. Among them, 3 rabbits in each group were euthanized after 6 weeks, and the remaining 7 rabbits were euthanized after 12 weeks. To evaluate the recruitment ability of the scaffold for MSCs, except for the blank group, 3 rabbits in each group were sacrificed one week after implantation, and the scaffold at the defect sites were collected for further analysis. All animals received feed and water without restriction, and were accommodated at 25 ℃ with a steady light/dark cycle. On

day 0, the rabbits were anesthetized with xylazine hydrochloride, tiletamine hydrochloride and zolazepam hydrochloride. After shaving and medical iodophor disinfection, the surface skin was cut open to expose the quadriceps. A 15 mm* 10 mm* 2 mm muscle block would be cut off in the middle of the quadriceps, and soaked in normal saline at 4 ℃ for preservation. After operation, the wound was sutured, disinfected, and injected with penicillin sodium to prevent infection.

The pure muscle samples were degreased, freeze-dried, and sterilized before implantation. Samples from GH, DI and NaOH groups were mineralized according to the above steps, followed by freeze-drying and sterilization. On day 4, the rabbits were anesthetized, and their right leg hair was removed, and disinfected, the epidermis was cut, and the muscle was separated with a support to expose the femur. A cuboid defect (8 mm* 5 mm* 1.5 mm) was created in the middle segment of the femur using a bone drill. Saline was added continuously during the drilling process to cool it down, and flush away the worn bone. The mineralized muscle scaffold was carefully placed into the corresponding rabbit defect area, that was to say, cutting muscle and implanting for bone repair were completed in the same rabbit. Then the muscle position was restored, and the skin wound was closed. Antibiotics were given three days after surgery to prevent infection. Rabbits were euthanized at 6 and 12 weeks postoperatively. The rabbit femurs were collected, and fixed in 4% paraformaldehyde for 1 week, and then micro-CT scan (resolution: 10 μm) was performed. The collected scanning data were imported into Milabs software for 3D visualization and bone repair index analysis.

After CT scan, the samples were decalcified by EDTA. Following paraffin embedding, samples were cut into sections (5 μm thick) along the center of the defect. HE and Masson stainings were used to evaluate the bone repair effect. Osteocalcin in new bone was labeled by osteocalcin Monoclonal Antibody (MA1-20788, Invitrogen™).

For MSCs recruitment *in vivo*, after fixation, decalcification, embedding and sectioning treatment, the MSCs in the scaffold were labeled by immunofluorescence staining. Retrieved sections were incubated with CD90 Monoclonal Antibody (MA181491, Invitrogen™) and CD44 Monoclonal Antibody (MA4400, Invitrogen™) overnight. After incubation with Donkey anti-Rat IgG (H+L) Highly Cross-Adsorbed Secondary Antibody (A48269, Invitrogen™) and Alexa Fluor® 594-conjugated AffiniPure Goat Anti-Mouse IgG H&L (HY-P8006, MedChemExpress) for 1 h and DAPI for 10 min at room temperature, the distribution of MSCs in the scaffold was observed under confocal microscopy (LSM900, ZEISS, Germany).

To evaluate the recovery of mechanical properties of the bone after 12 weeks, we performed a nanoindentation test (G200, Agilent) on the defect site, and compared it with the corresponding position of the intact left leg (n=3).

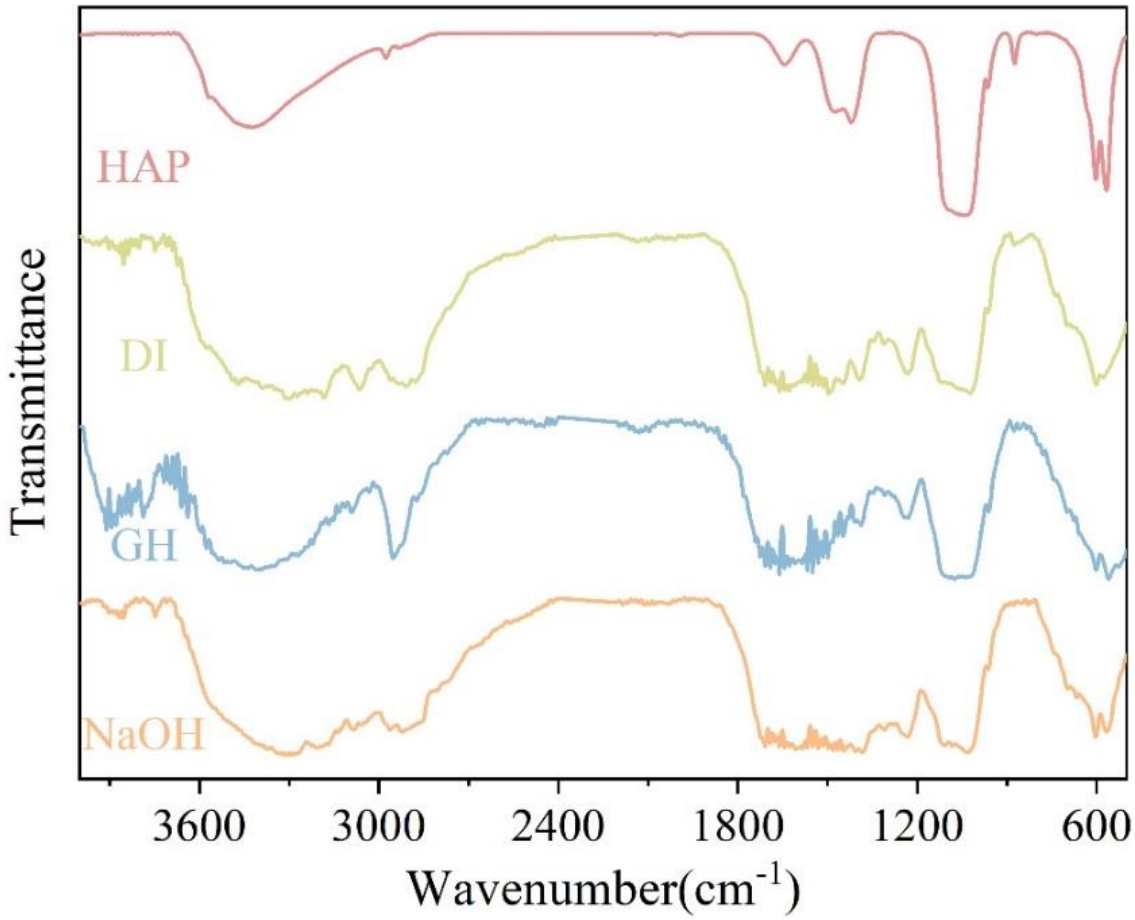

Fig. S1. FTIR spectrum of pure hydroxyapatite powder, DI group, GH group, and NaOH group.

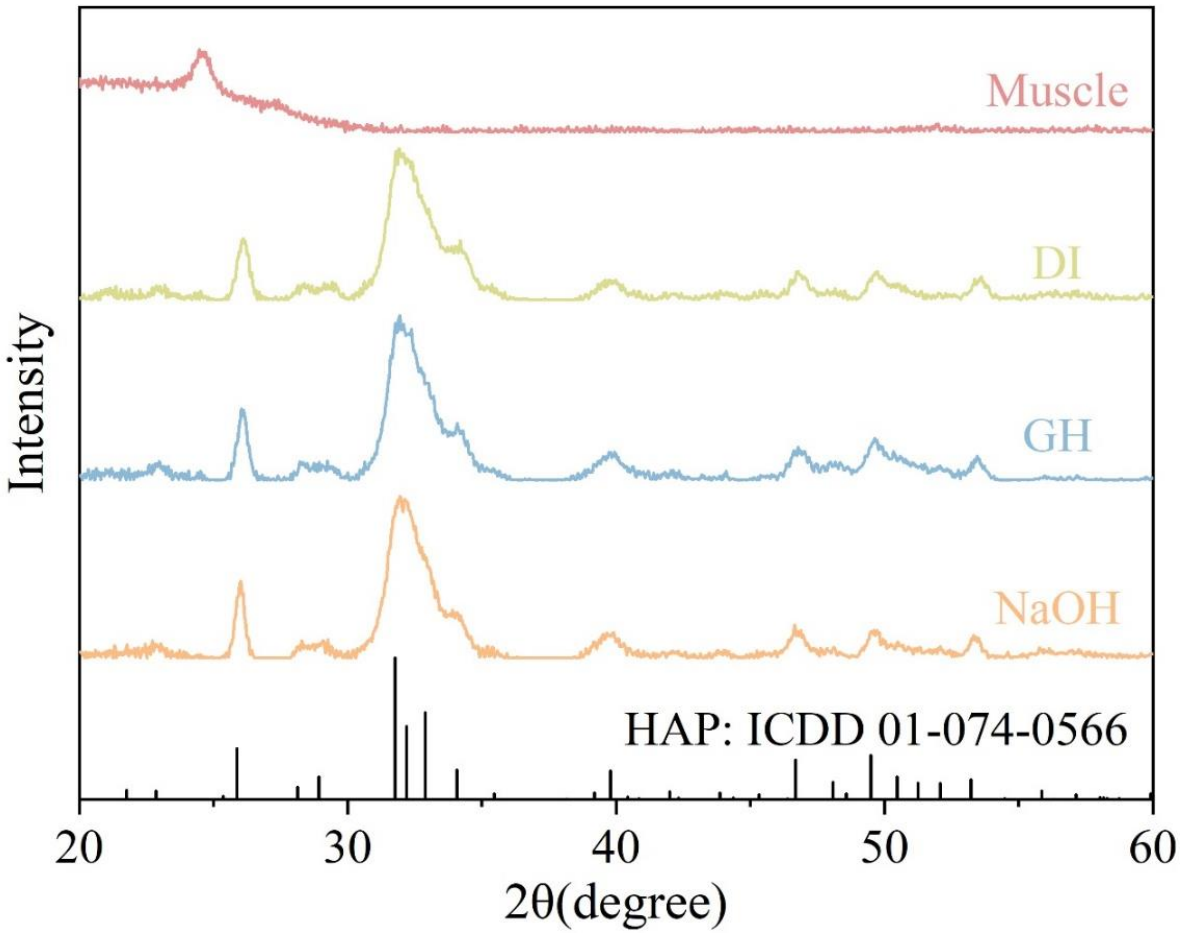

Fig. S2. XRD patterns of muscle, DI group, GH group, and NaOH group.

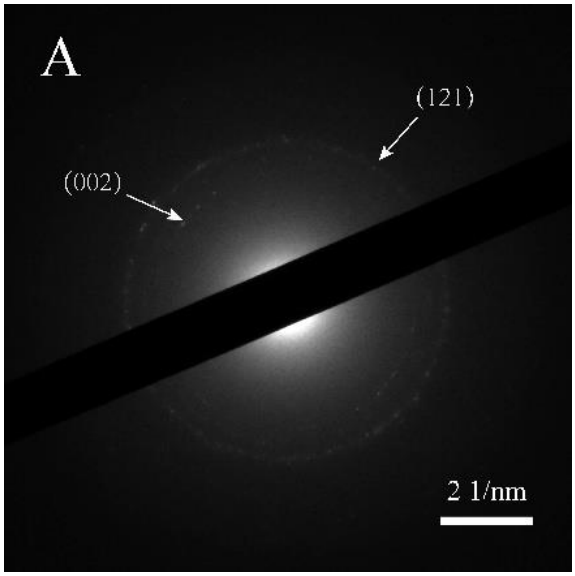

Fig. S3. SAED pattern of hydroxyapatite in GH group.

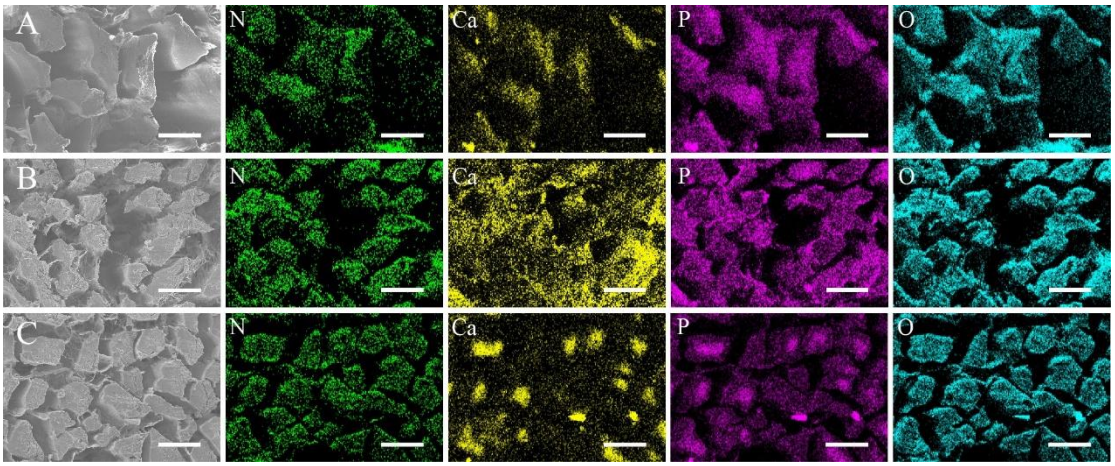

Fig. S4. A: SEM image and corresponding EDS mapping of GH group. B: SEM image and corresponding EDS mapping of NaOH group. C: SEM image and corresponding EDS mapping of DI group. Scale bars: 5μm.

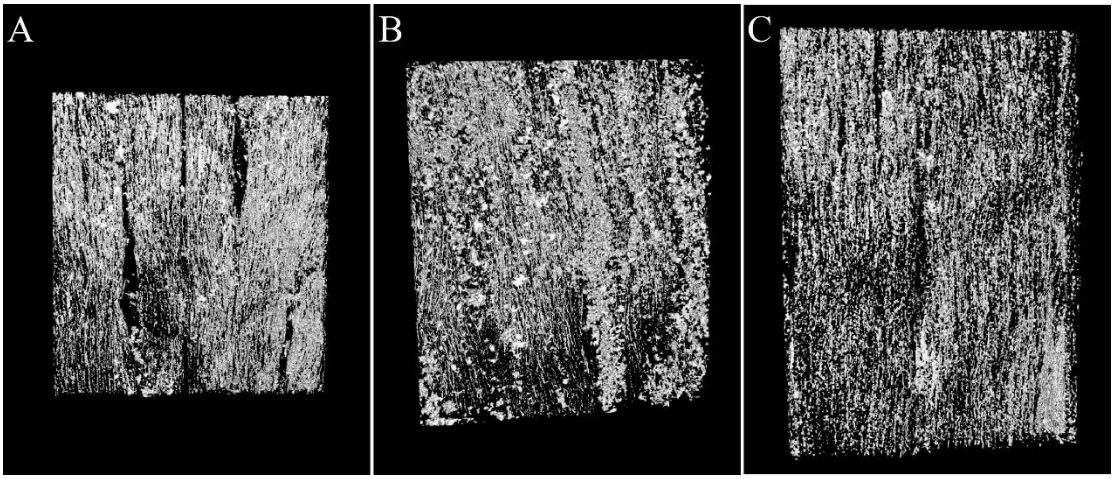

Fig. S5. CT images of different samples after mineralization. A: GH group; B: NaOH group; C: DI group.

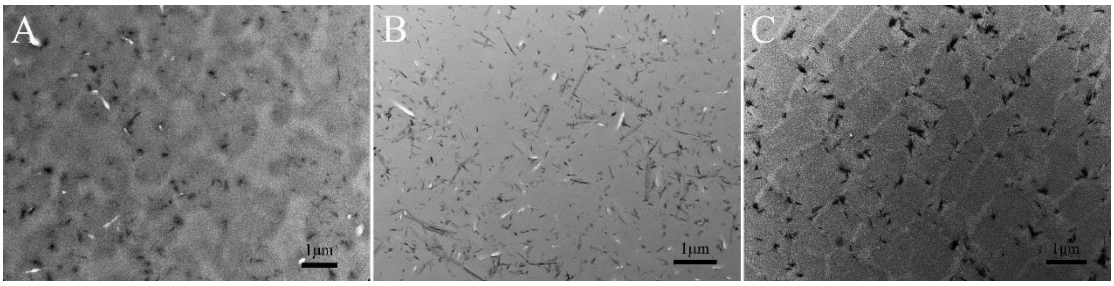

Fig. S6. TEM images that perpendicular to the direction of muscle fibers of different samples. A: GH group; B: NaOH group; C: DI group.

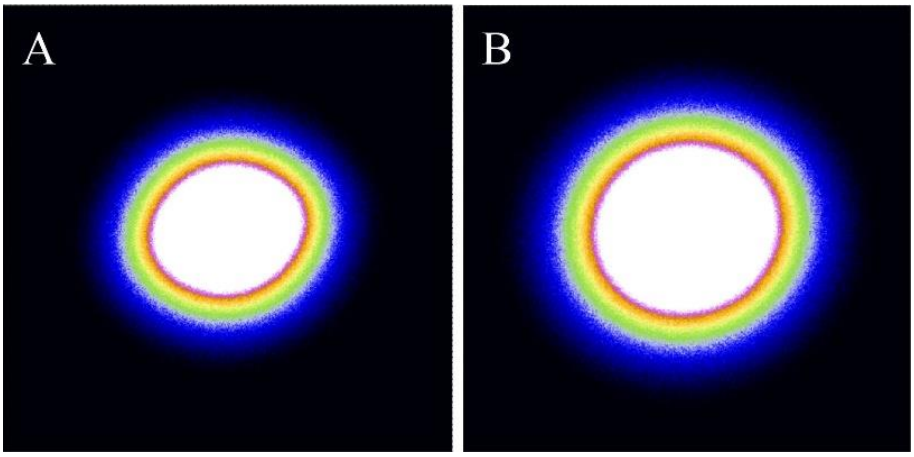

Fig. S7. 2D SAXS patterns of DI group (A) and NaOH group (B).

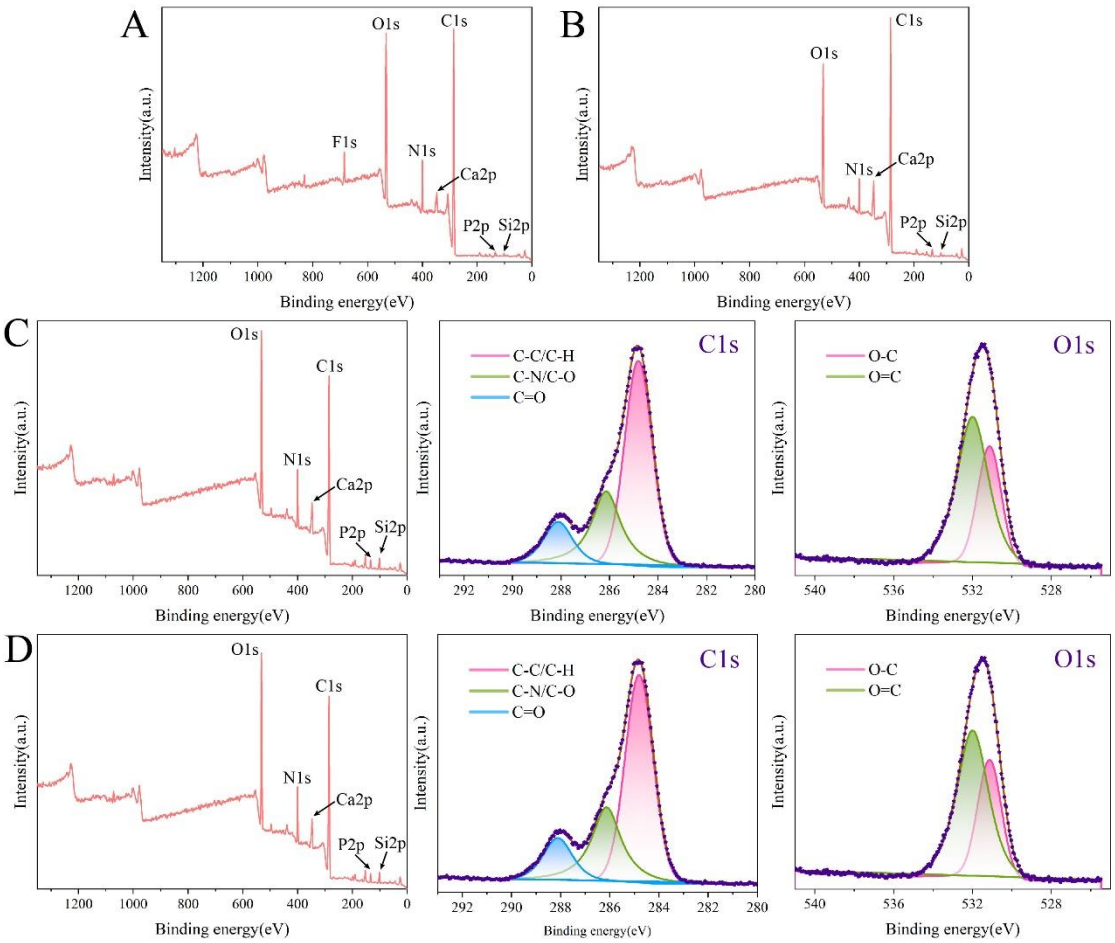

Fig. S8. A: Full scanning spectrum of X-ray photoelectron spectra of muscle; B: Full scanning spectrum of X-ray photoelectron spectra of GH group; C: Full spectrum, C1s and O1s spectra of high-resolution X-ray photoelectron spectroscopy of DI group; D: Full spectrum, C1s and O1s spectra of high-resolution X-ray photoelectron spectroscopy of NaOH group.

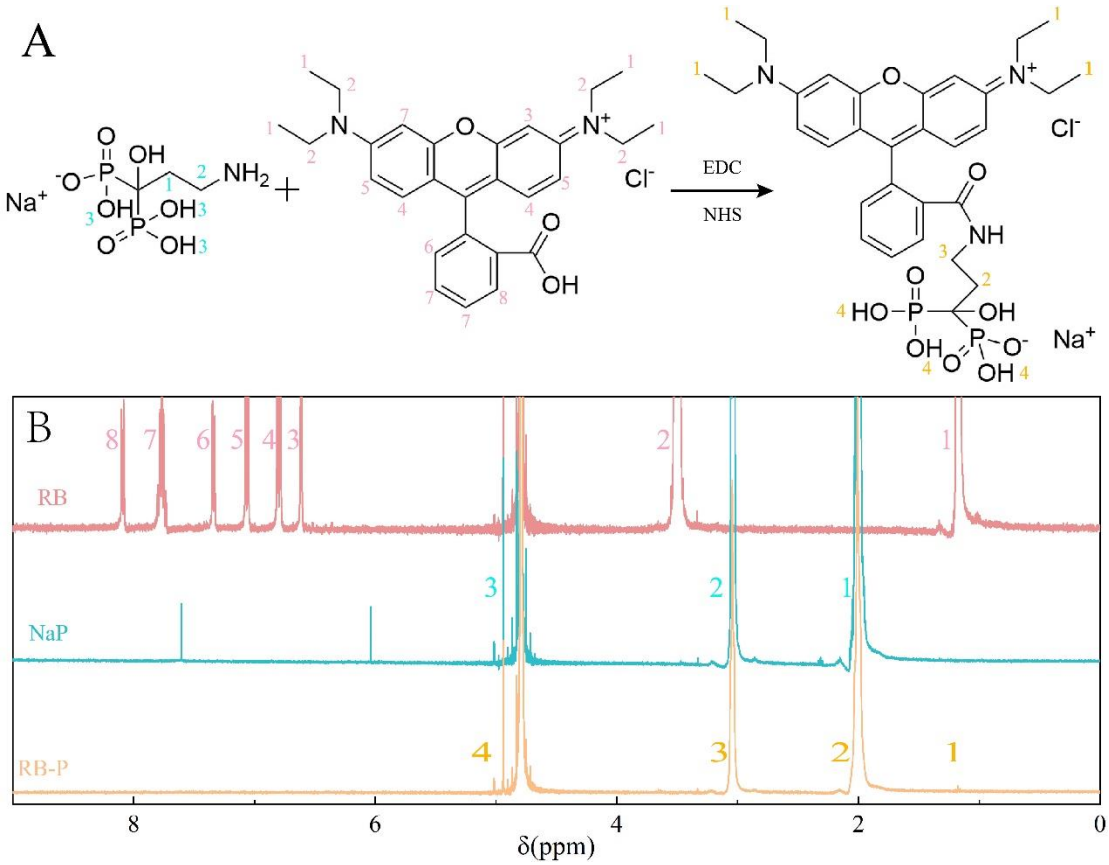

Fig. S9. A: Modification process of Rhodamine B; B: Nuclear magnetic spectra of rhodamine B (RB), sodium alendronate (NaP), and rhodamine B modified with sodium alendronate (RB-P).

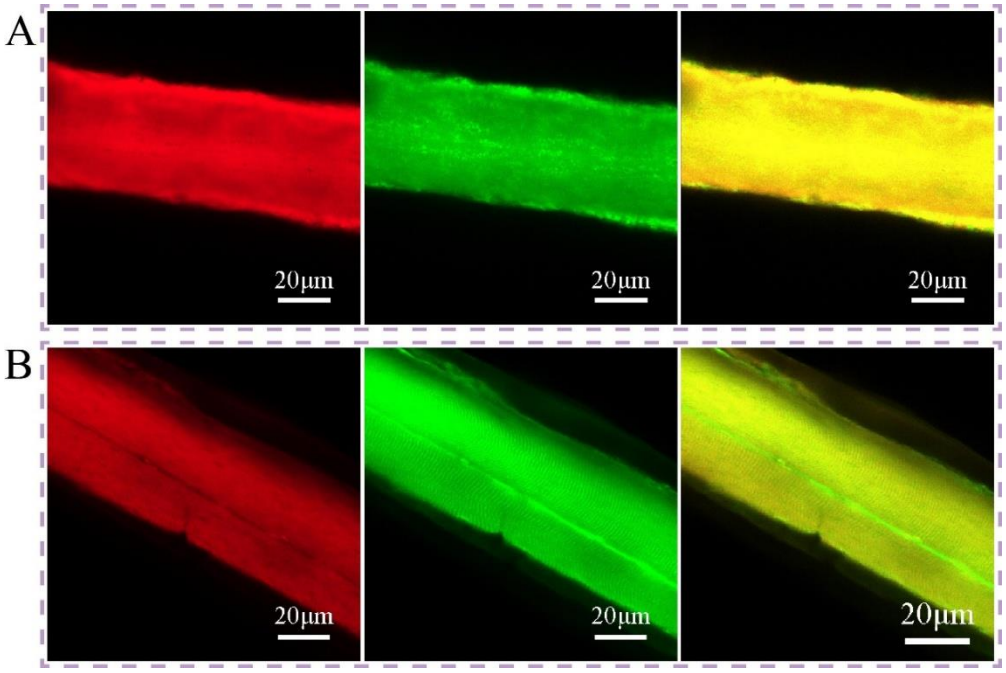

Fig. S10. Fluorescence staining photos of NaOH group (A) and DI group (B). The protein was stained red by CY5.5- NHS, while Ca^{2+} was marked green by rhodamine B modified with sodium alendronate. The fluorescence staining results indicated that hydroxyapatite was uniformly distributed within the myofibrils, which was consistent with the results obtained by TEM.

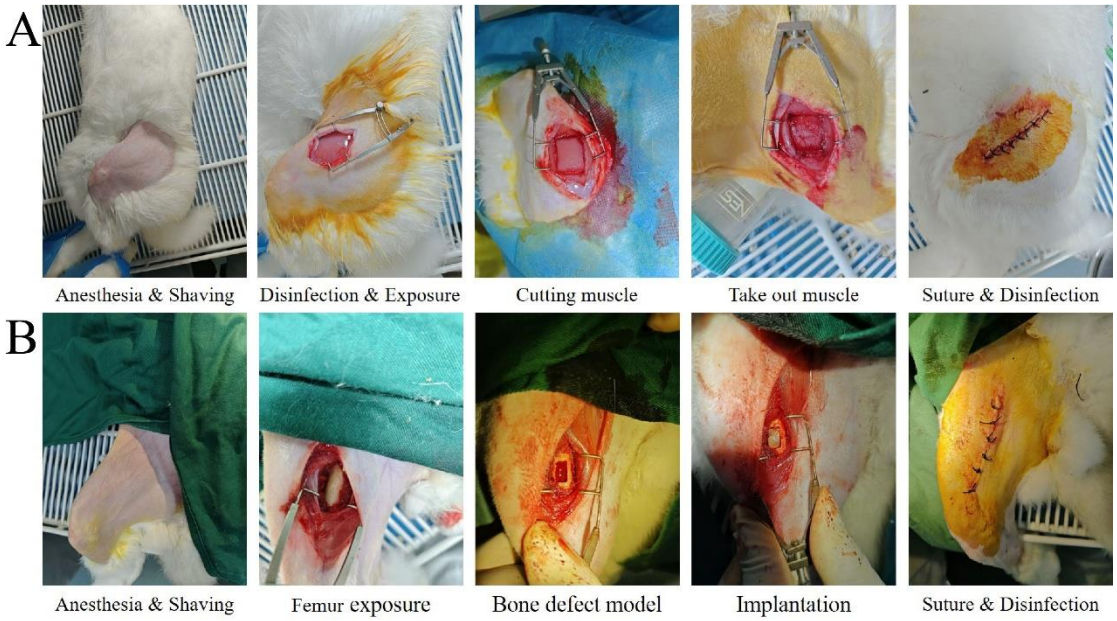

Fig. S11. Experimental procedures for muscle extraction(A) and bone defect implantation(B).

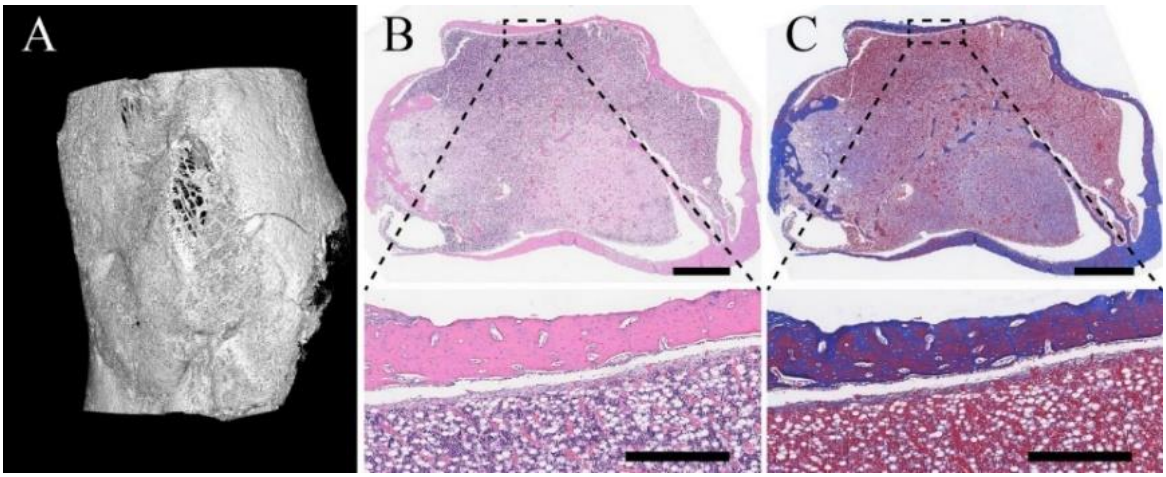

Fig. S12. Micro-CT images (A) of blank group after 12 weeks. H&E (B) and Masson (C) staining of the middle part of the defect (scale bar: 2 mm, scale bar in the enlarged image: 500μm).

Obvious cortical bone erosion occurred in the blank group after bone remodeling. Exposure of bone marrow in the blank group led to traumatic osteomyelitis, which eventually developed into osteonecrosis and fracture.

Fig. S13. (A-D) Digital photographs of rabbit femur regeneration after 12 weeks of implantation. A: GH group; B: NaOH group; C: DI group; D: pure muscle. The dotted orange box indicated the location of the defect.

Except for the GH group, the damaged areas in the other experimental groups still did not fully heal even after 12 weeks.

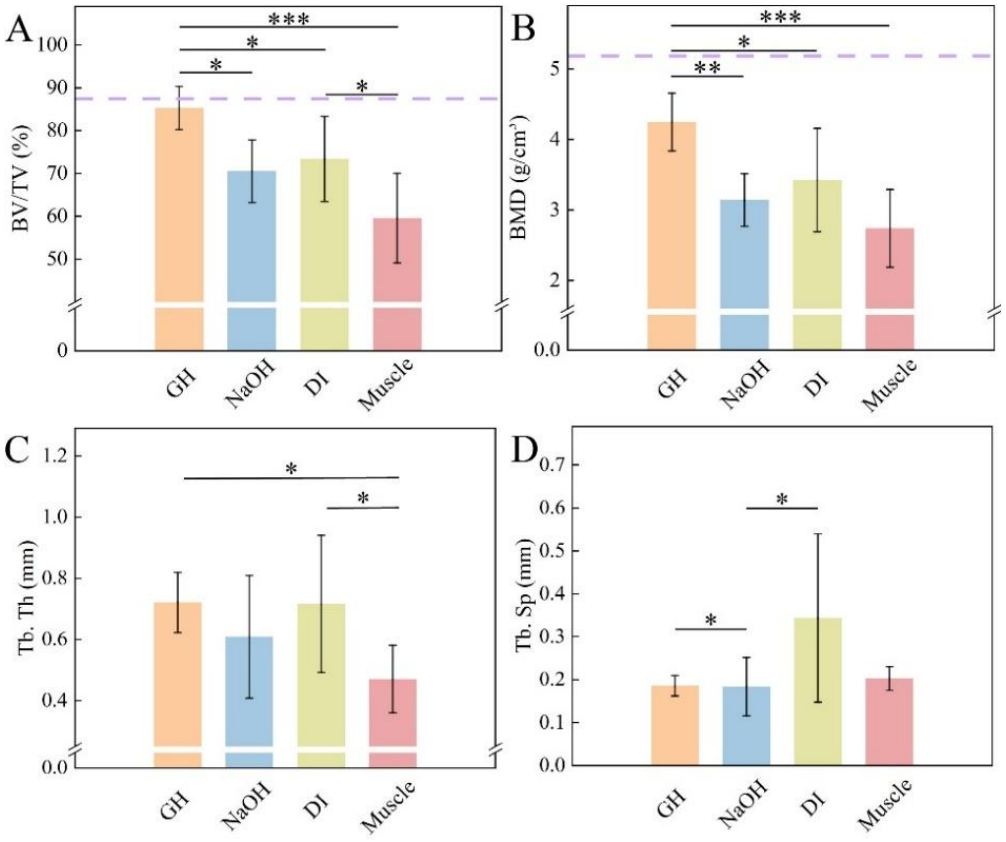

Fig. S14. (A) Bone volume/tissue volume (BV/TV), (B) bone mineral density (BMD), (C) thickness of trabecular (Tb. Th), and (D) trabecular bone separation (Tb. Sp) were calculated by Imalytics analysis software. In Fig. A and B, the relevant bone indicators of the intact left femur at the same position were marked with purple dotted lines.

After 12 weeks, the mineral content in the GH group recovered to over 90% of the initial level, and the bone mineral density also reached over 80% of that of normal femurs. Data was analysed from defects after 12 weeks in each group, as indicated in the bars ($n = 5$), and compared using one-way ANOVA analysis. *Significant difference with $P < 0.05$; ** Significant difference with $P < 0.01$; ***Significant difference with $P < 0.001$.

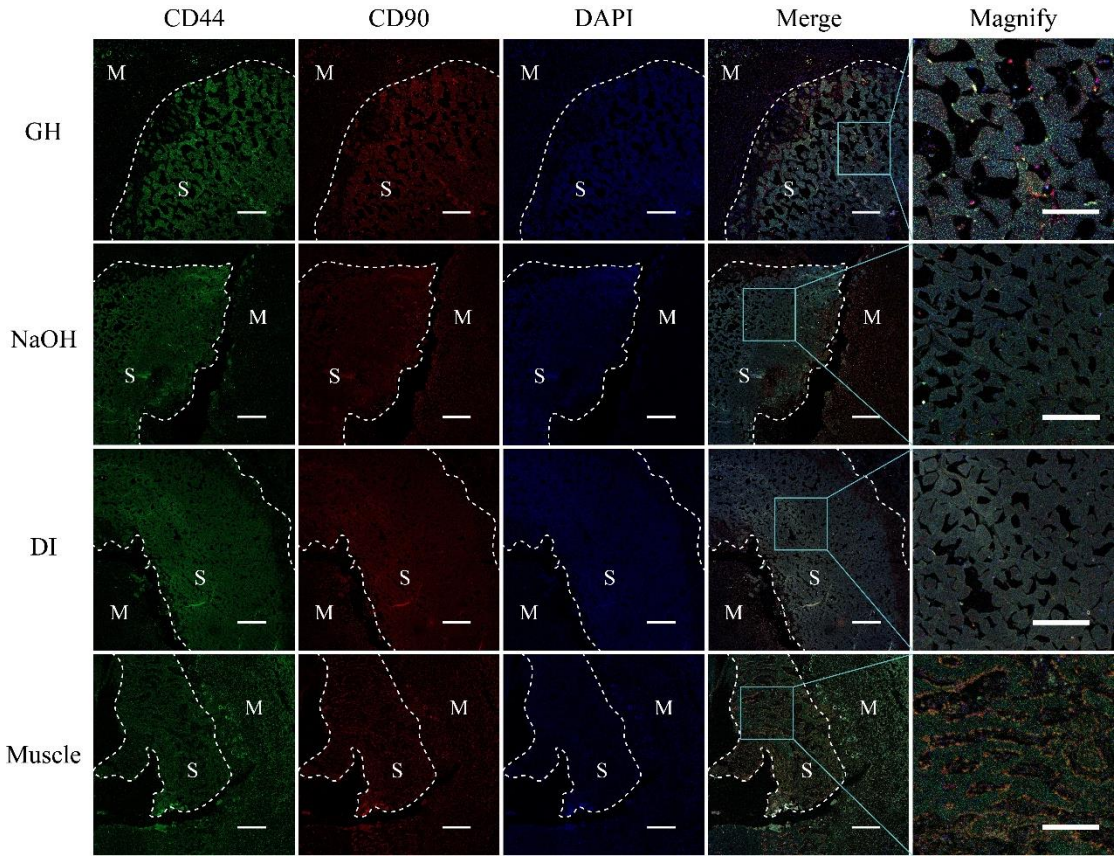

Fig. S15. The immunofluorescence staining results of MSCs in the scaffolds one week after implantation. According to relevant researches, cells residing on the implanted scaffolds were identified as MSCs when staining for the marker CD29 and CD90 were positive (M: marrow, S: scaffold, scale bars= 200μm, except scale bars in magnify image represented 100μm).

Among all the experimental groups, the GH group demonstrated the best MSCs recruitment: In the enlarged image, there were numerous CD44 and CD90 positive-expressing MSCs even at the center of the scaffold. The NaOH group and the DI group also exhibited a certain ability to recruit MSCs. However, the MSCs were concentrated at the contact sites between the scaffold and the bone marrow, and were rarely distributed within the scaffold. For the muscle group, due to the lack of inorganic calcium salts, there was no MSCs recruitment.

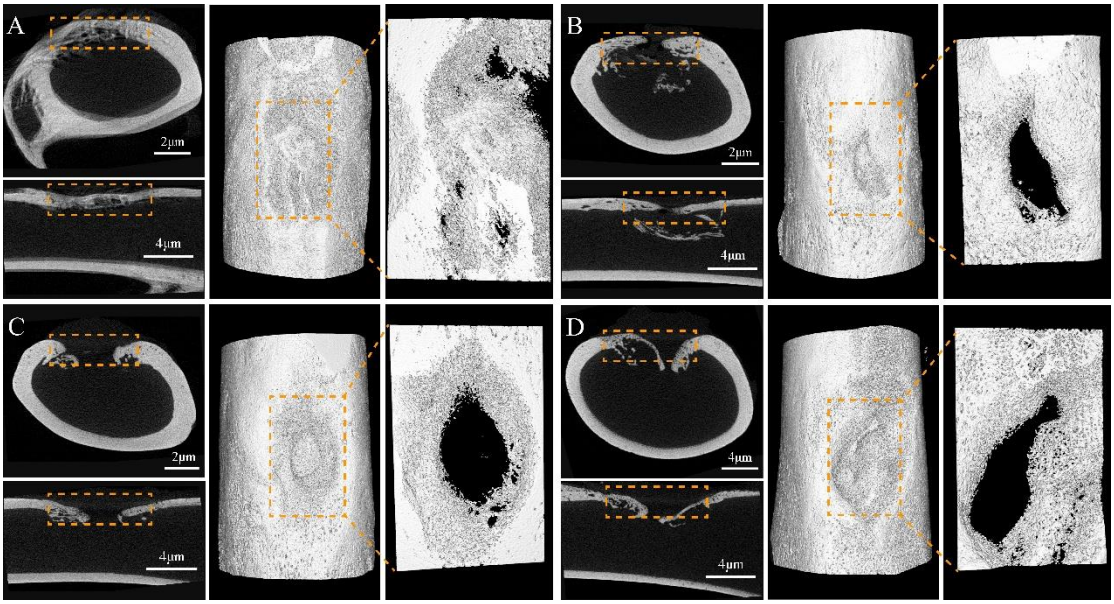

Fig. S16. Axial, sagittal, and 3D micro-CT images of rabbit femur regeneration after 6 weeks of implantation. A: GH group; B: NaOH group; C: DI group; D: pure muscle group. The dotted orange box indicated the location of the defect.

In GH group, the defect area had been largely covered by new bone tissue, with only a few localized pores remaining for repair. The other three groups exhibited the characteristic of gradually mineralizing from the defect margins towards the center, while the center of the defect remained completely empty. As the scaffold degraded, even though the defect center would gradually form bone, under the continuous compression from the external muscle, the new bone bended towards the side of the bone marrow, and could not restore its original shape.

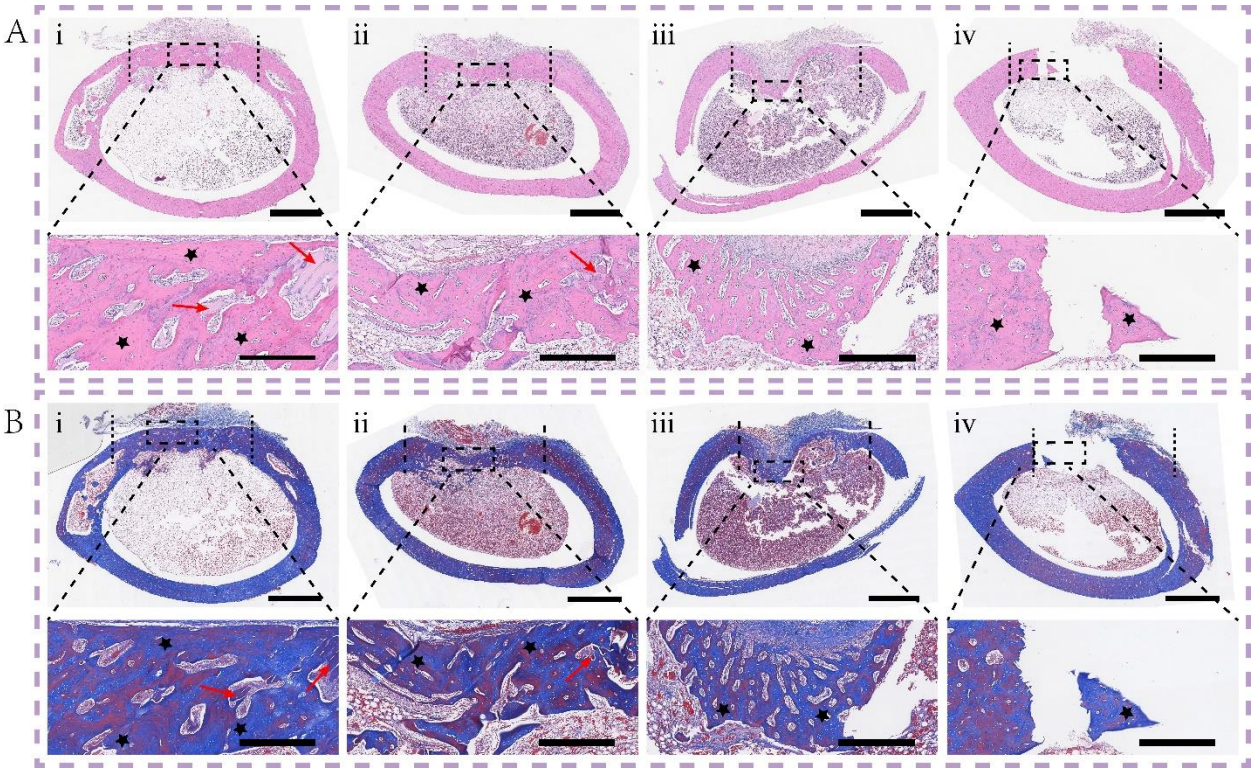

Fig. S17. H&E and Masson staining of each group at 6 weeks. Ai, Bi： GH group; Aii, Bii: NaOH group; Aiii, Biii: DI group; Aiv, Biv: muscle group. The initial defect area was marked by two vertical dashed lines (scale bar: 2 mm, scale bar in the enlarged image: 500 μm). Red arrows marked the remaining scaffolds, and black stars labeled the newly formed bones.

The staining results indicated that after 6 weeks, the scaffolds in the DI group and the Muscle group had completely degraded, which was not conducive to the maintenance and remodeling of the femoral morphology. For GH group, defect region was almost completely filled by new bone and residual scaffold, which could be attributed to the balance between the bone regeneration and the scaffold degradation, as well as the new pattern of uniform mineralization caused by the uniform distribution of MSCs within the scaffold.

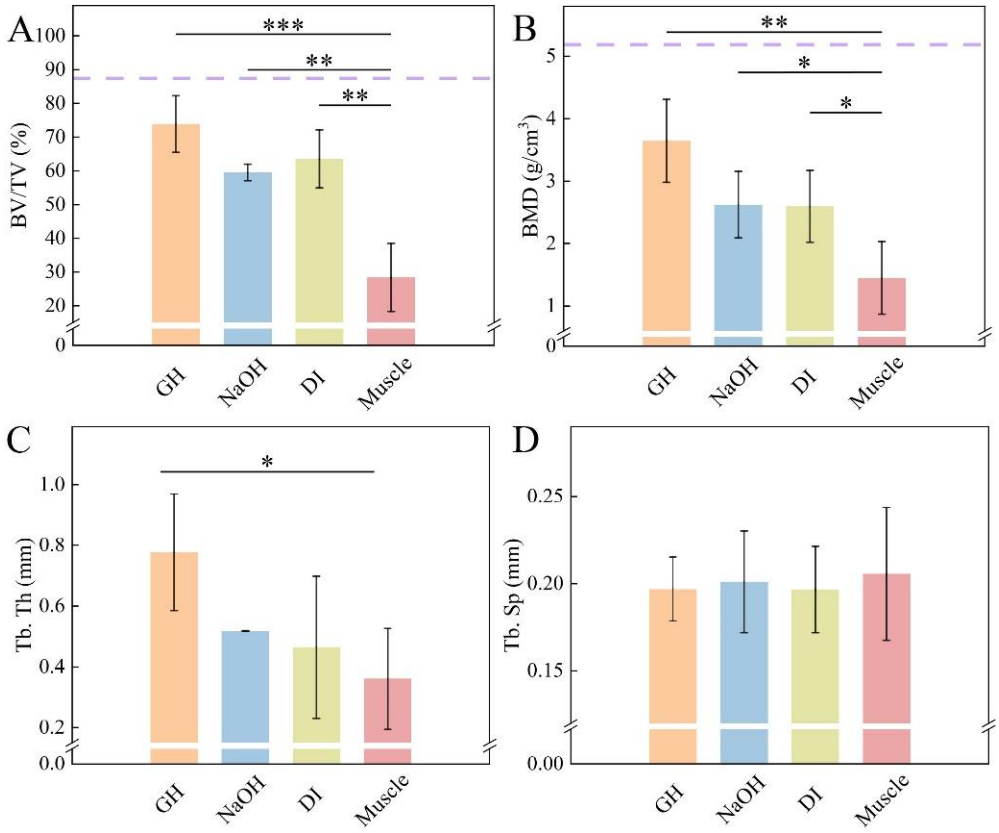

Fig. S18. (A) Bone volume/tissue volume (BV/TV), (B) bone mineral density (BMD), (C) thickness of trabecular (Tb. Th), and (D) trabecular bone separation (Tb. Sp) were calculated by Imalytics analysis software. In Fig. A and B, the relevant bone indicators of the intact left femur at the same position were marked with purple dotted lines. Except for the Muscle group, the other scaffolds could effectively accelerate the repair of bone defects within the first 6 weeks. Among them, the bone repair rate of the GH group was as high as 73.89%. Data was analysed from defects after 6 weeks in each group, as indicated in the bars (n = 3), and compared using one-way ANOVA analysis. *Significant difference with $P < 0.05$; ** Significant difference with $P < 0.01$; ***Significant difference with $P < 0.001$.

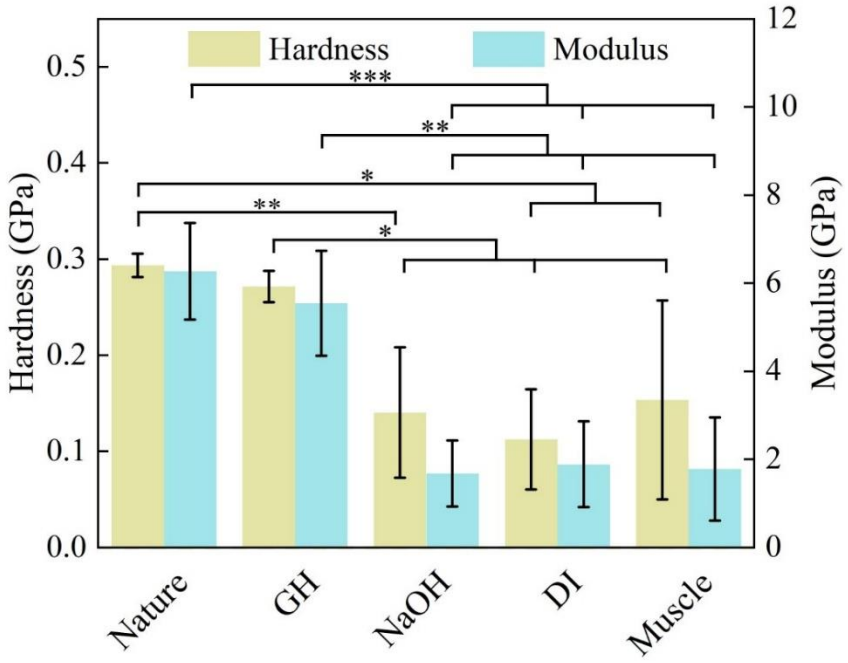

Fig. S19. Hardness and elastic modulus of the defect sites after 12 weeks measured by nanoindentation. As indicated in the bars (n = 3), data was compared using one-way ANOVA analysis. *Significant difference with $P < 0.05$; ** Significant difference with $P < 0.01$; ***Significant difference with $P < 0.001$.

Table S1. Effects of different scaffolds on bone defect repair

Materials	Bone defect model	Mechanism	Duration	Regeneration effect	Ref.
MXene film	Rat skull defect model (5mm)	Photothermal therapy	8 weeks	77.4 ± 3.5% (CT)	(*1*)
Mineralized collagen plywood	Metaphyseal bone defect of ewe (d: 8mm; h:13mm)	Hierarchical hybrid microstructure	2 months	54 ± 7% (scanner) 80 ± 12%(radiography)	(*2*)
Me/QCSGa-MOF@Cryogel[i]	Rat Model with Infected Distal-Femur Defect (d: 3mm; h: 3mm)	Antibacterial & radially oriented porous design	12 weeks	30%-40% (CT)	(*3*)
Silk fibroin	Pig tibial defects (d: 1cm; h: 1.1cm)	Lamellar-like porous design & MSCs loading	5 mouths	40%-50% (CT)	(*4*)
MgO_2/PLGA scaffold	Rat skull defect model (5mm)	Controllable releasing of Mg^{2+} and H_2O_2	12 weeks	30%-40% (CT)	(*5*)
Dense mineralized collagen	Rat distal femur defect model (d: 3mm; h: 4mm)	Hierarchical structure & high mineral content	12 weeks	40%-50% (CT)	(*6*)
Inorganic polyphosphate & CaP	Femur defect in osteoporosis mice (d: 2mm; h: 4mm)	Modulate energy metabolism	12 weeks	30%-40% (CT)	(*7*)
Chiral $Ca_2SiO_4.H_2O$ &bacterial cellulose	Humerus head drilling model in rat (No. 7-0 angle needle)	Si^{4+} and Ca^{2+} release; Chiral structures promote angiogenesis	12 weeks	50.17% ± 1.93% (CT)	(*8*)
PLGA/baicalein scaffold	Rat skull defect model (5.5mm)	Hierarchical porous structure & baicalein	8 weeks	24%-32% (CT)	(*9*)
PU-CaGP[ii] / intestinal alkaline phosphatase	Rat skull defect model (5mm)	Enzyme regulate the Ca-P microenvironment	12 weeks	20%-30% (CT)	(*10*)
Silk fibroin/ MgO scaffold	Rat skull defect model (4mm)	Water-responsive shape-memory & Mg^{2+}	8 weeks	27.2 ± 0.64% (CT)	(*11*)

Zn-Li alloy scaffolds	Rat model of femoral condyle defect (d: 3mm; h: 4mm)	High strength & immunomodulation effects (Zn^{2+}, Li^{+})	3 mouths	2%-3% (CT)	(*12*)
ZOL-PLGA@Yoda1/SPIO[iii]	Osteoporosis mouse skull defect model (5mm)	Bone targeting and magnetic targeting; Yoda1 activate Piezo1	8 weeks	30%-35% (CT)	(*13*)
Sodium hyaluronate/alendronate sodium/$CaCl_2$	Rat skull defect model (5mm)	Sustained release of alendronate sodium	4 weeks	～20% (CT)	(*14*)
DL@etBC scaffold[iv]	Rat skull defect model (5mm)	Local chemoimmunotherapy	8 weeks	～10% (CT)	(*15*)
PEGS-PGA/SeSe/Rapa hydrogel[v]	Aged mice with distal femoral defects (1.2mm)	Eliminates ROS & delays senescence	8 weeks	35.82% ± 5.71% (CT)	(*16*)
nHAp@PDA/chitosan	Full-thickness rabbit cranium defect (10mm)	Oriented porous structure	12 weeks	10%-15% (CT)	(*17*)
BP@PDA/AlgMA/ECM[vi]	Rat femoral defect (d: 3mm)	Electrical stimulation	6 weeks	40%-60% (CT)	(*18*)
GelMA/hypoxia-triggered exosome-mimetics	Rat skull defect model (5mm)	Higher content of pro-angiogenic genes	12 weeks	23.06 % ± 0.91 % (CT)	(*19*)

i：A cryogel compased of GelMA and hydroxyapatite nanoparticles that loaded with quaternized chitosan (QCS) coated gallium-based metal–organic framework and Methicillin (Me); ii: Calcium glycerophosphate modified polyurethane; iii: Zoledronate (ZOL)-decorated PLGA@Piezo1-activated molecule Yoda1/superparamagnetic iron oxide; iv: 3D-printing etched $Ca_3(PO_4)_2$ scaffold modified with Lactobacillus rhamnosus GG (LGG) biofilm and loaded with doxorubicin (Dox); v: PEGylated poly(glycerol sebacate) (PEGS-NH2)/poly(γ-glutamic acid) (γ-PGA) hydrogel (PEGS-PGA) loaded with poly(diselenide-carbonate) nanomicelles (Se) containing rapamycin (R); vi: Polydopamine-modified black phosphorus nanosheets/alginate methacryloyl/extracellular matrix.

Movie S1. Mineralization process of muscle fibers for NaOH group.

Movie S2. Mineralization process of muscle fibers for GH group.

Movie S3. Mineralization process of muscle fibers for DI group.

Movie S4. Expansion of muscle fiber after the introduction of Ca^{2+}.

Movie S5. CT reconstruction results of femoral defect site after 12 weeks (GH group).

Movie S6. CT reconstruction results of femoral defect site after 12 weeks (NaOH group).

Movie S7. CT reconstruction results of femoral defect site after 12 weeks (DI group).

Movie S8. CT reconstruction results of femoral defect site after 12 weeks (Muscle group).

References and Notes

1. S. Wan *et al.*, Scalable ultrastrong MXene films with superior osteogenesis. *Nature* **634**, 1103-1110 (2024).
2. M. Robin *et al.*, Mineralized collagen plywood contributes to bone autograft performance. *Nature* **636**, 100-107 (2024).
3. Y. Liu *et al.*, Directional Freeze-Casting Cryogel Loaded with Quaternized Chitosan Modified Gallium Metal–Organic Frameworks to Capture and Eradicate the Resistant Bacteria for Guided Regeneration in Infected Bone Defects. *Advanced Materials* **37**, 2414437 (2025).
4. Y. Shuai *et al.*, Oriented Cortical-Bone-Like Silk Protein Lamellae Effectively Repair Large Segmental Bone Defects in Pigs. *Advanced Materials* **37**, 2414543 (2025).
5. C. Li *et al.*, Time-Sequential and Multi-Functional 3D Printed MgO2/PLGA Scaffold Developed as a Novel Biodegradable and Bioactive Bone Substitute for Challenging Postsurgical Osteosarcoma Treatment. *Advanced Materials* **36**, 2308875 (2024).
6. L. Kong *et al.*, Multiscale engineered artificial compact bone via bidirectional freeze-driven lamellated organization of mineralized collagen microfibrils. *Bioactive Materials* **40**, 168-181 (2024).
7. X. Cheng *et al.*, Energetic Calcium Phosphate Nanominerals for Osteoporosis Treatment. *Advanced Functional Materials* **35**, 2415906 (2025).
8. Z. Cai *et al.*, Hierarchical Chiral Calcium Silicate Hydrate Films Promote Vascularization for Tendon-to-Bone Healing. *Advanced Materials* **36**, 2404842 (2024).
9. M. Zhang *et al.*, Personalized PLGA/BCL Scaffold with Hierarchical Porous Structure Resembling Periosteum-Bone Complex Enables Efficient Repair of Bone Defect. *Advanced Science* **11**, 2401589 (2024).
10. Q. Zhao *et al.*, Self-Activating Phosphorus-Rich Substrate Import Enzyme Catalytic Domains for Bone Regeneration. *Advanced Functional Materials* **34**, 2316428 (2024).
11. Z. Mao *et al.*, Mechanically robust and personalized silk fibroin-magnesium composite scaffolds with water-responsive shape-memory for irregular bone regeneration. *Nature Communications* **15**, 4160 (2024).
12. S. Li *et al.*, Multiscale architecture design of 3D printed biodegradable Zn-based porous scaffolds for immunomodulatory osteogenesis. *Nature Communications* **15**, 3131 (2024).
13. H. Guan *et al.*, Magnetic Aggregation-Induced Bone-Targeting Nanocarrier with Effects of Piezo1 Activation and Osteogenic–Angiogenic Coupling for Osteoporotic Bone Repair. *Advanced Materials* **36**, 2312081 (2024).
14. J. Liu, X. Zhang, C. Xiao, X. Chen, A Drug-Mineralized Hydrogel Orchestrated by Spontaneous Dynamic Mineralization. *Advanced Functional Materials* **34**, 2311844 (2024).
15. H.-Y. Gu *et al.*, Probiotic Biofilm Modified 3D-Printing Scaffolds for Improving Chemo-Immunotherapy of Bone Tumor and Promoting Osteogenesis. *Advanced Functional Materials* **34**, 2311015 (2024).
16. Z. He *et al.*, Rejuvenating Aged Bone Repair through Multihierarchy Reactive Oxygen Species-Regulated Hydrogel. *Advanced Materials* **36**, 2306552 (2024).
17. X. Li *et al.*, Engineered Microchannel Scaffolds with Instructive Niches Reinforce Endogenous Bone Regeneration by Regulating CSF-1/CSF-1R Pathway. *Advanced Materials* **36**, 2310876 (2024).

18. T. Wang *et al.*, Rehabilitation exercise–driven symbiotic electrical stimulation system accelerating bone regeneration. *Science Advances* **10**, eadi6799 (2024).
19. Z. Zhong *et al.*, Hypoxia-triggered exosome-mimetics accelerate vascularized osteogenesis. *Materials Today* **73**, 16-29 (2024).